Eng. Sci., 2020, 10, 85–94

Engineered Science

DOI: https://dx.doi.org/10.30919/es8d1005

Experimental and Theoretical Characteristic of Single Atom Co-N-C Catalyst for Li-O_2 Batteries

Gaoyang Li,[#,1] Congcong Dang,[#,1] Yue Hou,[2] Feng Dang,[1,*] Yuqi Fan,[3,*] and Zhanhu Guo[4]

Abstract

Single atom Co-N-C can be used as a low-cost cathode catalyst for Li-O_2 batteries (LOBs) with abundant highly active sites and high efficient atom utilizations. In the present work, hierarchical porous single atom Co-N-C catalyst was prepared through acid etching from a Co/Co-N-C intermediate, featuring an efficient slack of volume expansion, easy mass transmission via the interconnected carbon-framework, and sufficient surface area to accommodate discharge products. The single atom Co-N-C catalyst exhibited a superior catalytic capacity for LOBs with a large specific capacity of 14075 mAh g^{-1} and a long cycle life of 340 cycles. The oxygen reduction reaction (ORR) / oxygen evolution reaction (OER) mechanisms of the discharge products of single atom Co-N-C catalyst were identified by using density functional theory (DFT) calculations, showing avenues for improving the future design of single atom catalyst.

Keywords: Li-O_2 battery; Air cathode; Single atom Co-N-C catalyst; DFT calculation.
Received: 21 April 2020; Accepted: 8 May 2020
Article type: Research article

1. Introduction

Li-O_2 batteries (LOBs) owning to their high specific capacity and theoretical energy density up to 3600 Wh kg^{-1}, far more than that of Li-ion batteries (LIBs), are considered as the most promising candidate for next generation energy storage devices.[1-3] The sluggish kinetics of LOBs includes oxygen reduction reaction (ORR) in the discharge procedure and oxygen evolution reaction (OER) in the subsequent charge procedure. In a typical electrochemical reaction, Li ions from Li anode pass through the electrolyte, accept electrons and combine with oxygen from the external environment at the cathode to form Li_2O_2 during discharging (ORR). While charging (OER), the Li_2O_2 is reversibly decomposed into oxygen and Li ions.[4,5] However, complicated triple-phase regions with the coexistence of solid, electrolyte and gas, as well as the insoluble and insulating nature of the discharge products of Li_2O_2 along with parasitic reactions, result in inferior rate capability, low round trip energy efficiency and poor cycling stability, which hinder the applications of Li-O_2 batteries.[6-8]

To tackle these problems, intensive efforts have been devoted to explore oxygen cathodes with functional structures and/or superior ORR and OER catalytic properties. A dramatic oxygen cathode of LOBs needs a high ORR/OER catalytic capability, porous structure to accommodate more discharge products for high energy density and superior electrical conductivity. Carbon-based materials with high electric conductivities and designed functional structure are firstly used to catalyze electrode reaction and achieve innovative breakthrough in improving the performance of LOBs.[9-11] Other than this, their complex tunnel structure can provide space to support diffusion of O_2 and Li^+ ions. Meanwhile, carbon-based materials are usually inactive to the OER reaction.[12] In response, intense efforts have been made to explore better performing catalysts. Precious metals (such as Pt, Ru, Pd, and Ir) have been regarded as ideal cathode catalysts for LOBs.[13-16] Carbon supported precious metal cathodes can effectively catalyzing the formation and decomposition of

---

[1] *Key Laboratory for Liquid-Solid Structural Evolution and Processing of Materials (Ministry of Education), Shandong University, 17923 Jingshi Road, Jinan 250061, China*
[2] *Department of Materials Science and Engineering, City University of Hong Kong, Tat Chee Avenue, Kowloon, Hong Kong, P.R. China*
[3] *Institute of Environment and Ecology, Shandong Normal University, Jinan, 250014, China*
[4] *Integrated Composites Laboratory (ICL), Department of Chemical & Biomolecular Engineering, University of Tennessee, Knoxville, TN 37996, USA.*
[#] *These authors contributed to this work equally.*
* ***E-mail**: dangfeng@sdu.edu.cn, yuqifan@sdnu.edu.cn*

Li_2O_2. However, their unstable catalytic nature and high cost limit their commercial application. Alternatively, carbon supported transition metals (M = Co, Fe, Ni, etc.) and their heteroatom (N, O, S, P, etc.) coordinated catalysts are promising substitutes because of the synergistic effects originating from abundant chemical defects and maximized catalytic active sites.[17-19] Some works have demonstrated that Co or Fe nanocrystal anchored N doped carbon nanocomposites containing both M (M=Co, Fe) and M-N-C high active sites exhibited a superior electrocatalytic performance in non-noble metal catalyst for energy storage and electrochemical conversion.[20,21] Compared with precious metal catalysts, the durability of these M/M-N-C catalysts cannot satisfy the needs of long-time cycles. Theoretical prediction indicated that M-C bond possesses a higher activity than the transition metal atoms in the ORR/OER process of LOBs. Fabrication of single atom M-N-C catalyst is a reasonable pathway to obtain high performance LOBs system.[22,23]

For a Co-N-C single atom catalyst, it possesses the advantages including low cost, high atom utilization, abundant active site exposure and low-coordination. Transition metal atoms can be anchored on N doped carbon matrix through chemical bonding forming $Co-N_4$ active sites, which are active for oxygen adsorption and subsequent O=O bond breaking.[24] Some works have demonstrated the outstanding catalytic performance of single atom catalysts on the applications of hydrogen evolution, CO_2/O_2 reduction, dye-sensitized solar cells and energy storage.[25-28] Meanwhile, to our best acknowledge, there is no report on the successful application of single atom catalyst for LOBs.

Herein, hierarchical porous Co-N-C single atom catalyst was fabricated to satisfy the demands of highly efficient cathode catalysts for LOBs, featuring an efficient slack of volume expansion, easy mass transmission via interconnected carbon-framework, sufficient surface area to accommodate discharge products in microstructure, and high atom utilization, and abundant highly active site exposure in the catalytic capability. The evenly distributed $Co-N_4$ bond serves as single atom active sites for the ORR/OER process in LOBs, prevents the unrestricted growth of Li_2O_2 and accelerates the decomposition of Li_2O_2 films. It is found that the single atom Co-N-C cathode exhibits superior catalytic capability and cycle stability for LOBs. Theoretical simulation indicated the reaction mechanism of discharge products during the ORR/OER process and identified the low overpotential of single atom Co-N-C catalyst. On the other hand, the weak chemical adsorption of discharge products may limit its superior cycle stability at a low fixed capacity.

2. Experimental section

2.1 Material preparation

0.12 g SiO_2 nanoparticles were added into 5 mL deionized water, then the mixture was ultrasonic stirred until SiO_2 was dispersed in the deionized water evenly. Then 0.3 g agar, 1.5 g urea and 0.3 g $Co(NO_3)_2 \cdot 6H_2O$ were added and magnetic stirred for 10 minutes. After a while, the mixture turned to be gel. Then the gel was kept in the freeze dryer for 24 hours in order to remove solvent. The dried precursor was sintered at 1100 °C for 2 hours in N_2 atmosphere with a heating rate of 5 °C min^{-1}. The carbonized material was added into hydrofluoric acid (HF) for removing SiO_2 and cobalt particles. After acid etching, the material was washed several times by deionized water and dried in a Blast drying oven overnight. Then atomic cobalt anchored in the N-doped carbon sphere (ACo-NC) was obtained. The controlled adding amount of $Co(NO_3)_2 \cdot 6H_2O$ for different groups was 0, 0.2, 0.3, and 0.4 g respectively, and the obtained materials were named NC, ACo-NC-1, ACo-NC-2, ACoNC-3 respectively.

2.2 Material characterization

The morphologies and elemental distribution are provided by scanning electron microscopy (SEM, JSM- 7800F), and transmission electron microscopy (TEM, JEOL2100F). The phase composition was analyzed using X-ray diffraction (XRD, Rigaku D/Max-rB) with a Cu-Kα radiation at a voltage of 40 kV and a current of 40 mA. Raman was conducted by Renishaw inVia confocal Raman microscope. The chemical composition was catalyzed by X- ray photoelectron spectroscopy (XPS, Thermo ESCALAB 250XI). Thermogravimetric analysis (TGA) was conducted to ensure the content of Cobalt by TGA/DSC1 1600. The specific area and pore size distribution were determined by Brunauer-Emmett-Teller (BET).

2.3 Assembly and electrochemical measurement

The working electrode was composed of CoNC material, Ketjen Black (KB) and poly (tetrafluoroethylene) (PTFE), which were ultrasonically mixed with a mass ratio of 4:4:2 and then covered on a carbon paper. In order to remove the isopropanol, the electrode was heated in vacuum oven at 120 °C for 10 hours before assembly process. The $Li-O_2$ cell contains Li anode, glass fiber separator, active material coated cathode, and electrolyte composed of 1M lithiumbis (trifluoromethanesulfonyl) (LiTFSI) in tetraethylene glycol dimethyl ether (TEGDME). The loading mass of cathode catalyst was measured as ~1 mg by a high-precision balance. All the batteries were assembled in a glove box full filled with Ar atmosphere, both the water content and oxygen content were controlled below 0.1 ppm.

All the electrochemical measurements of $Li-O_2$ batteries were carried on a sealed bottle filled with oxygen. Galvanostatic discharge/charge tests were carried out on LAND CT 2001A multi-channel battery tester. The specific capacity and current were determined by the weight of active material. The cyclic voltammograms (CV) and electrochemical impedance spectroscopy (EIS) measurements were tested on an electrochemical workstation (PARSTAT MC) at a scan rate of 0.1 mV s^{-1} under the limited potential range of 2.35 to 4.35 V versus Li/Li^{+}. To investigate the decomposition of the discharge product, differential electrochemical mass spectrometry (DEMS) system was used to study the evolution rate of O_2, CO_2, and H_2O during the charging process. During the charging process, high- purity Ar was used as the carrier gas for quantifying the evolution of O_2. The flow rate of purge gas was typically 1.43 mL min^{-1}. The cell was tested under a current density of 200 mA g^{-1} with a limited capacity of 500 mAh g^{-1}.

2.4 DFT Calculation

All data of calculation was obtained by Vienna Ab Initio Simulation Package[29,30] based on density functional theory (DFT). The projector augmented wave method was used to describe the electron-ion interaction. The electron exchange and correlation energy were treated by the Perdew-Burke-Ernzerh (PBE) function[31] of the generalized gradient approximation (GGA). The cut-off energy is set to 400 eV and a 3x3x1 k-point grid generated by the gamma-centered Monkhorst-Pack approach. The criterion of force relaxation and energy for structural relaxation is 0.02 eV/Å and 10^{-4} eV, respectively. The vacuum layer is considered to be ~15 Å on each side. Similar models and parameters have been used in catalytic reaction calculations.[32,33] Gibbs free energy[34,35] and Bader charge analysis[36-38] have also been successfully applied.

3. Results and discussion

A schematic illustration of the synthesis process of Co-N-C single atom catalyst is presented in (Fig. 1). A hard template method was employed to synthesize the hierarchical porous single atom Co-N-C catalyst. SiO_2 spheres with a diameter of 400 nm were used as hard templates to create porous structure, were first mixed in an agar solution containing $Co(NO_3)_2$ and solidified to prepare the agar gel matrix. Followed by freeze drying, the SiO_2 spheres were pressed to form ordered aggregate structure due to the shrinkage of the gel matrix.[39] After carbonization under N_2 atmosphere, hierarchical porous single atom Co-N-C catalyst was acquired after removing the SiO_2 spheres and extra Co element by HF treatment. Co atom and N element formed the single atom active catalytic Co-N_4 sites, which could promote the adsorption of O_2 and the fracture of O=O bond during oxygen reduction reaction.[24] Co/Co-N-C before acid etching (nano Co-NC) were also prepared to compare the catalytic capacity of the single atom Co-N-C catalyst.

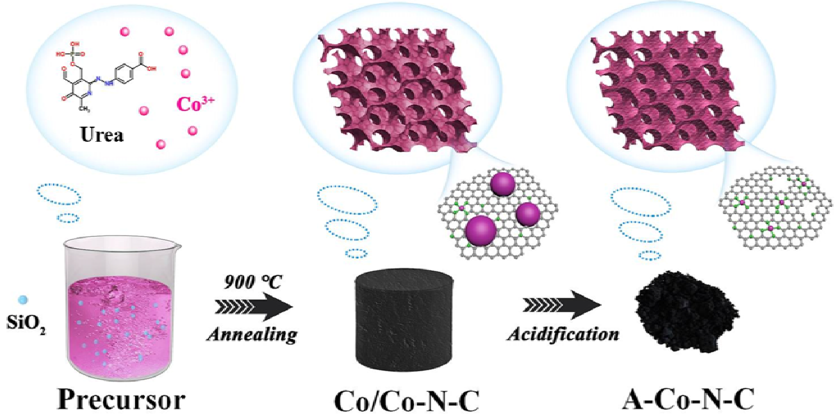

Fig. 1 Schematic illustration of synthesis process of ACoNC catalyst

SEM and TEM were carried out to reveal the morphology and microstructures. A honeycomb-like architecture with homogeneous micropores of 400 nm in size was observed in (Fig. 2a-b). A rough surface (Fig. 2a) and some carbon bulges (Fig. S1) were observed on the carbon shell compared to the initial Co/Co-N-C processor before acid etching (Fig. S2). The element mapping (Fig. S3) indicated uniform distribution of Co and N elements. The selected area electron diffraction (SAED) pattern (inset of Fig. 2b) shows the diffraction rings corresponding to the (002) plane of C. The thickness of the carbon wall was about 10 nm as shown in (Fig. 2d). The interplanar spacing (Fig. 2d) was 0.35 nm, which corresponded to the (002) plane of graphite. It's worth mentioning that no Co nanoparticles were observed from SEM and TEM observations.

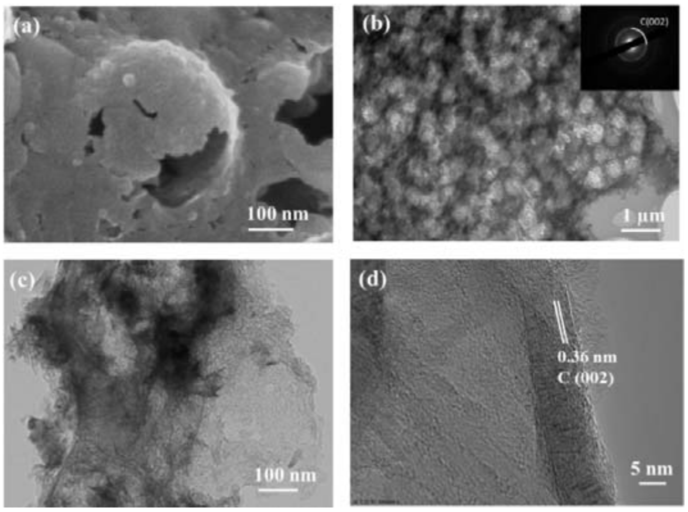

Fig. 2 (a) SEM image and (b-d) TEM images of ACoNC-2 catalyst.

High-angle annular dark-field scanning transmission electron microscopy (HAADF-STEM) was carried out to reveal the existence of atomic Co and shown in (Fig.). Plenty of bright dots are observed in (Fig. 3a), corresponding to Co atoms. The uniform distribution of these bright spots indicates the uniform distribution of cobalt atom. The element mappings of Co, C, N element are displayed in (Fig. 3b). It can be concluded that all of Co, N and C elements are distributed in the composite uniformly.

(Fig. 4a) shows the XRD pattern of ACo-N-C samples. Before acid etching, the diffraction peaks at 44.2° were matched well to the (111) plane of Co (PDF#15-0806).[40] After acid etching, no peaks belong to Co were detected. The detected diffraction peak at 26° indicates the existence of the graphite phase, while the peak at 43.4° corresponds to the (103) plane of carbon (PDF#26-1083). It can be seen that the peak of graphitic carbon in ACo-N-C samples is stronger than that in N doped carbon, which indicates a high graphitic ratio with an enhanced electrical conductivity. The Raman spectra were also carried out to evaluate the graphitization of ACo-N-C and shown in (Fig. 4b). The D band located at about 1340 cm^{-1} corresponds to disorder and amorphous carbon, while the G band at about 1578 cm^{-1} represents the sp^2 hybridized graphitic carbon atoms.[41-43] The numerical values of the four samples are 0.72, 0.60, 0.61 and 0.92, respectively. The decreased I_D/I_G ratio of ACoNC-1, 2 compared to that of N doped carbon indicated that the decoration of Co atoms decreased the defects carbon matrix and enhanced the degree of graphitization. However, a high concentration of Co atom would decrease the degree of graphitization.

The content of Co atom in the ACo-N-C was measured using TG analysis and shown in (Fig. 4c). The ACo-N-C samples were heated at 790 ℃ in the air for 2h at a heating rate of 5 ℃/min. After heating, Co was oxidized in air and only Co_3O_4 was maintained. The content of Co in ACoNC-1, ACoNC-2, ACoNC-3 was calculated to be 0.53, 1.50 and 3.19 wt%, respectively. These results indicated that the content of Co in ACoNC can be controlled through the addition of Co source in the synthesis process. N_2 adsorption/desorption isotherm curve (Fig. 4d) was conducted to determine

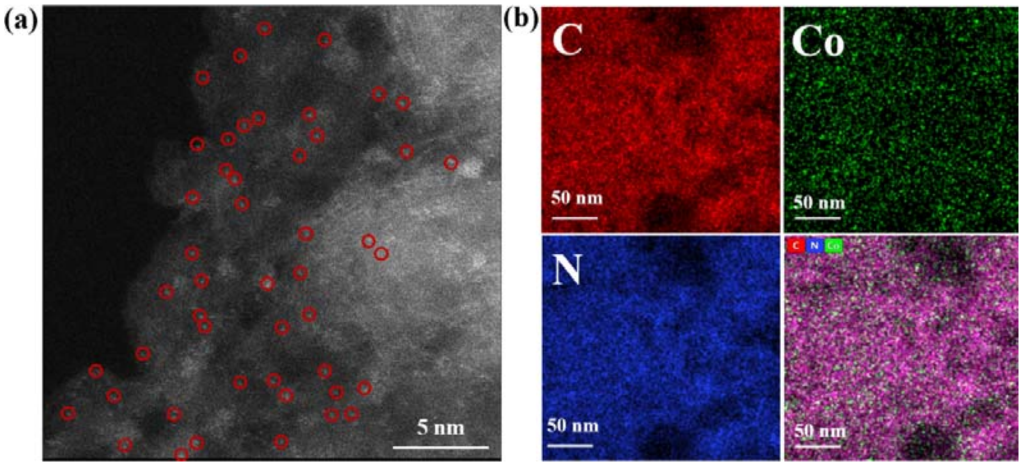

Fig. 3 (a) HAADF-STEM image and (b) EDS mapping of Co, N and C element accompany with their superimposed image of ACoNC-2.

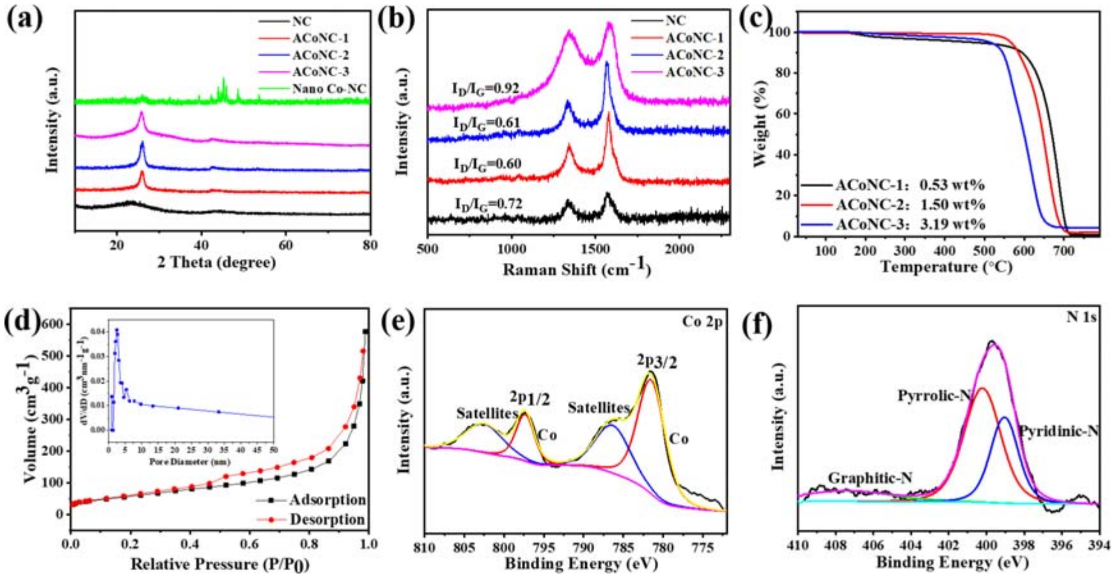

Fig. 4 (a) XRD pattern, (b) Raman pattern and (c) TGA curves of the ACoNC catalyst; (d) BET and pore size distribution of ACoNC-2; High-resolution XPS spectra of (e) Co 2p and (f) N 1s of ACoNC-2. accompany with their superimposed image of ACoNC-2.

the specific surface area of the ACoNC-2 sample, The nitrogen adsorption/desorption isotherm curves indicated an H3 hysteresis loop typical of Type IV mesoporous structure.[44-46] The specific surface area was determined to be 213.983 m^2/g. This result means more active sites for oxygen attachment and generation and decomposition of discharge products. We can also observe that the main pore diameter is located around 2.39 nm. Mesopores not only serve as the channels for the transport of Li^+ and O^{2-}, but also provide enough active sites for discharge products.

XPS analysis was conducted to explore the chemical composition of the catalyst. As shown in (Fig. S8), the XPS survey spectrum of ACoNC-2 displayed the Co 2p, O 1s, N 1s, C 1s and Si 2p peaks. There were still Si and O residues because the reaction in the HF treatment might not be complete. In the high-resolution spectrum of Co 2p (Fig. 4e), the curve can be deconvoluted into four peaks. The peak at 781.5 eV accompanied with a satellite peak at 786.3 eV is assigned to Co 2p3/2, while the peak at 797.3 eV with a satellite peak at 802.5 eV is associated with Co 2p1/2.[47-49] This result indicated the existence of CoO atom in the ACo-N-C catalyst. The high resolution of N 1s (Fig. 4f) can be deconvoluted to four peaks, 398, 398.9, 399.9 and 401 eV, corresponding to Pyridinic-N, Co-Nx, Pyrrolic-N and Graphitic-N, respectively.[50, 51] The contents of Pyridinic-N and Pyrrolic-N are 48.44% and 5.06%, respectively, calculated based on the XPS spectra. Pyrrolic-N attaches to the carbon atom in the matrix while pyridinic-N mostly exist in the form of Co-N_4 active sites.[24] Pyridinic-N and Pyrrolic-N have a superior adsorption ability of ORR intermediates of LOBs than that of graphitic-N (9.09%).[41] The content of Co-Nx was identified as 37.42% which confirmed the bonding between Co atoms and N element.

The oxygen electrode consisted of ACo-N-C catalyst and KB with a weight ratio of 1:1 as an electrical conductor. In rechargeable LOBs with 1.0 M LiTFSI/TEGDME electrolyte, the CV curve of ACoNC-2 in (Fig. 5a) showed both distinct higher cathodic ORR (at 2.6 V) and anodic OER (at 3.6 V) current peaks with a Co content of 1.5 wt%. Meanwhile, the ACoNC-1 and ACoNC-3 electrodes exhibited almost the same OER current peaks at 3.4 V, and ORR discharge platforms at around 2.6 V, similar to those of NC and KB (2.6 V). Furthermore, the CV curve of nano Co-NC shows inferior electrochemical catalytic performance in which both cathodic and anodic current values are weak. It indicated that the OER and ORR processes are hindered in the nano Co-NC electrode, which may be attributed to the large particle size of Co.

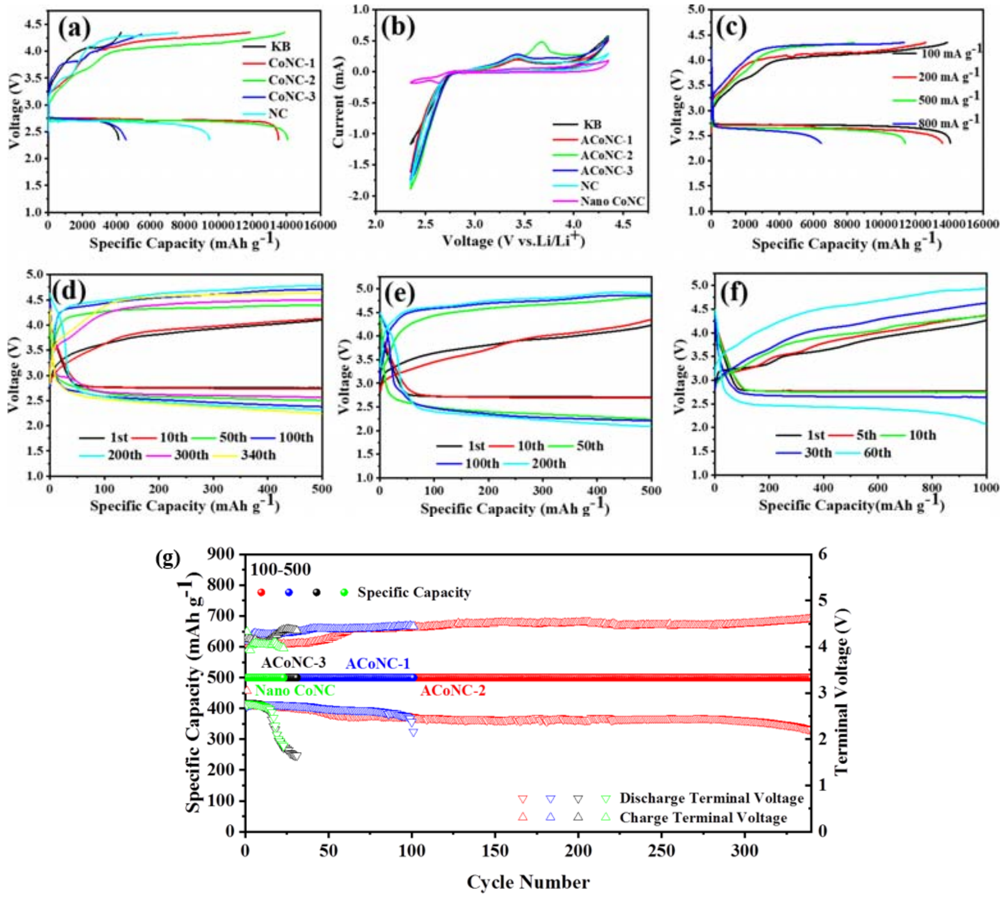

Fig. 5 (a) CV curves and (b) initial discharge/charge profiles of ACoNC eletrode; (c) rate performance of ACoNC-2; Typical discharge/charge profiles of ACoNC-2 with (d) 500 mAh g^{-1} at 100 mA g^{-1}; (e) 500 mAh g^{-1} at 200 mA g^{-1}; (f) 1000 mAh g^{-1} at 500 mA g^{-1}; (g) cycling performance and the corresponding charge/discharge profiles of ACoNC and nano Co-NC catalyst; (d) BET and pore size distribution of ACoNC-2; High-resolution XPS spectra of (e) Co 2p and (f) N 1s of ACoNC-2 accompany with their superimposed image of ACoNC-2.

The galvanostatic discharge/charge test was conducted under the current density of 100 mAh g^{-1}. As (Fig. 5b) shows, ACoNC-2 electrode displayed the largest discharge capacity of 14075 mAh g^{-1}. The discharge capacity decreased to 13544 mAh g^{-1} as the amount of Co doping was reduced to 0.53% (ACoNC-1). However, the specific capacity of ACoNC-3 electrode with the largest Co content was decreased sharply to 4573.25 mAh g^{-1}, even less than that of NC electrode (9485.75 mAh g^{-1}). Besides, the charging platform of only 4 V for theACoNC-2 is the lowest among all the samples, it can be concluded that the OER performance of ACoNC-2 is superior to other samples. This is due to appropriate content of active sites and porous structures of the sample, in which the discharge product can be adsorbed efficiently.

The rate performance of ACoNC-2 electrode was tested at the current densities of 100, 200, 500 and 800 mA g^{-1}, respectively. As shown in (Fig. 5c), the discharge specific capacities of ACoNC-2 were 14075, 13603 and 11414 mAh g^{-1}. Furthermore, it can retain a high specific capacity of 6466 mAh g^{-1} even at a high current of 800 mA g^{-1}. It indicated the ACoNC-2 catalyst obtained outstanding rate performance and electrochemical stability. As shown in (Fig. 5d), the ACoNC-2 catalyst could run 340 cycles with a fixed capacity of 500 mAh g^{-1} at the current density of 100 mA g^{-1}. Discharge and charge platforms after 340 cycles are maintained at 2.3 and 4.5 V, respectively. Even under the current density of 500 mAh g^{-1} with a cut-capacity of 500 mAh g^{-1}, it still could operate 200 cycles (Fig. 5e). We further improved the cut-off specific capacity to 1000 mAh g^{-1} under a current density of 200 mA g^{-1}, only 60 cycles were obtained (Fig. 5f). The cycle performance decreased with the increase of limited capacity at the current density of 100, 200 and 500 mA g^{-1} for ACoNC catalyst. Meanwhile, the cycle life of ACoNC-1 and 3 was only 98 and 31 cycles with a cut-off capacity of 500 mAh g^{-1} at 100 mA g^{-1} as shown in (Fig. 5g) and S4. The nano Co-NC electrode also delivered an inferior cycle performance with a cut-off capacity of 500 mAh g^{-1} at 100 mA g^{-1}. The discharge voltage decreased to 1.85 V only after 23 cycles.

To further identify the mechanism of electrochemical reaction, DEMS (Fig. 6) was applied to figure out the gas evolution during charge process[52,53] with a fixed specific capacity of 500 mAh g^{-1} at a current of 200 mA g^{-1}. The curves of O_2, CO_2 and H_2O were selected from the gas mixture. The relevant calculation was conducted following Equations (1-3):

$$Q=I\times t \tag{1}$$

$$v(e^{-})=Q\times e^{-1}, \tag{2}$$

$$v(O_2)=Gas\ Evol.Rate/60.NA \tag{3}$$

The typical "M" shape of O_2 evolution curve was obtained. The O_2 evolution rate increased apparently at state I during charge process. In this progress, O_2 was mostly derived from the decomposition of $Li_{2-x}O_2$, which was the intermediate product during discharge progress. Then, the production rate of O_2 was decreased gradually, it corresponded to the consumption of $Li_{2-x}O_2$.[54-56] When the charge voltage reached 4.1 V, the O_2 evolution rate increased again owning to the decomposition of Li_2O_2 at a higher voltage. The calculation data also confirmed this result. The number of electrons passing in per second during charging were identified as 3.12×1015. Two points were selected to calculate the ratio of v(e^-) and v(O_2) as p1 and p2. The ratio of p1 was calculated as 1.03 while that of p2 was 1.92. According to different ratios of e^- and O element in $Li_{2-x}O_2$ and Li_2O_2, it can be concluded that P1 corresponded to the decomposition of $Li_{2-x}O_2$ while P2 was attributed to the decomposition of Li_2O_2. It is worth mentioning that both CO_2 and H_2O did not show any peaks in the whole charge process, which indicated that no side reaction occurred during the discharge process. The above results confirmed good electrochemical performance of the ACoNC material.

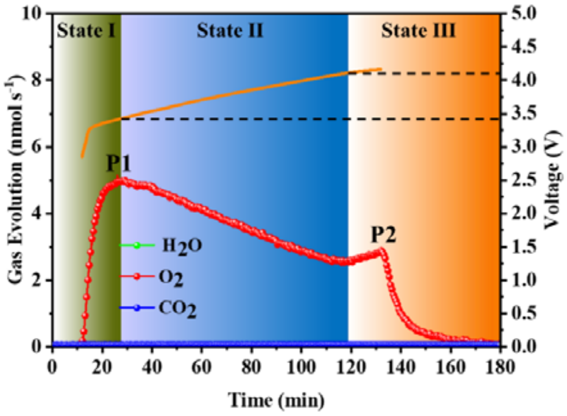

Fig. 6 In-situ DEMS profiles of ACoNC-2 during charge process with a fixed capacity of 500 mAh g^{-1} at 200 mA g^{-1}.

The products in the process of charge and discharge reactions were also characterized. S1, S2, S3 and S4 states correspond to the initial-discharge state (state 1), fully discharged state (state 2), initial-charged state (state 3) and fully charged state (state 4). As shown in the XRD pattern (Fig. 7b), in state 1, the peaks of Li_2O_2 started to appear, when the cell was fully discharged, the strong peaks of Li_2O_2 were observed (state 2). When the batteries were in the charge process, the signal of Li_2O_2 began to be weakened and finally disappeared after fully charged, which was attributed to the decomposition of Li_2O_2.

EIS (Fig. 7c) was conducted to explore more about the reaction kinetics. The test results are related to the characteristics of intrinsic charge transfer and charge transport kinetics of batteries. The diameter of semicircle is connected with the electron transfer resistance.[57-59] As shown in (Fig. 7c), after discharge, the electron impedance of the battery was increased significantly from 70 to 237 Ω. The increase of electron impedance was due to the deposition of insulated discharge products. After recharge, the diameter of the semicircle became smaller again with the decomposition of discharge products. Even when after

100 cycles, the EIS was still maintained at 118 Ω, which was quite lower than that after discharge. These results also confirmed the stable cycle ability of the ACoNC catalyst.

The electrode morphology during discharge/charge process was observed by SEM. (Fig. S5) shows the SEM image of fresh electrode with the honeycomb-like structure of ACoNC powders. After fully discharged (Fig. 7d), some lamellar discharge product was observed on the surface of the spherical shell, which was identified as the discharge product Li_2O_2 by XRD result. After galvanostatic charged (Fig. 7e), these slices completely disappeared. Even after 100 cycles, the electrode maintained the initial morphology as shown in (Fig. 7f). It indicated the revisable stability of ACoNC catalyst.

Furthermore, ex-situ high-resolution XPS spectra of Li 1s were detected (Fig. S6) for the S1, S2 and S3 states in (Fig. 7a). At the initial process of discharging, the main peak of Li_2O_2 (~55.4°) corresponding to a weak peak of $Li_{2-x}O_2$ (~56.1°) were detected, which indicated that the Li_2O_2 was the main discharge product and LiO_2 was the mediate discharge product at the initial stage of discharge.[60,61] When further discharged to 500 mAh g^{-1}, the peak of $Li_{2-x}O_2$ disappeared and the intensity of Li_2O_2 peak still increased, demonstrating the formation of Li_2O_2 film. It is worth mentioning that the peak of $Li_{2-x}O_2$ reappeared during the initial charging process. With charging to the limited capacity of 500 mAh g^{-1}, both peaks of $Li_{2-x}O_2$ and Li_2O_2 decreased apparently, which were ascribed to the decomposition of the discharge product.

Density functional theory (DFT) calculations based on the first-principles were used to investigate the positive step reactions of single atom catalyst in LOBs.[62-65] The calculated free energy diagrams of the catalytic process at different potentials and reaction processes are shown in (Fig. 8). First, the reaction paths of the ORR and OER processes were calculated. The corresponding adsorption energy and charge transfer numbers are listed in Table S1. Because of a very weak adsorption effect (E_{ads} = -0.02 eV) of Li on the Co-N_4 active sites and the higher O_2 adsorption energy (E_{ads} = -2.19 eV), the adsorption of O_2 molecules occurred firstly in the ORR process as shown in (Fig. 8b), and then the Li_2O_2* (E_{ads} = -0.97eV) formed through the intermediate of LiO_2*, where * indicates the molecules adsorbed on the surface. The reasonable reaction path is listed as following Equations(4-6):

$$O_2 \rightarrow O_2^* \tag{4}$$

$$Li^+ + O_2^* \rightarrow LiO_2^* \tag{5}$$

$$Li^+ + LiO_2^* \rightarrow Li_2O_2^* \tag{6}$$

Correspondingly in the OER process, the delithiation of Li_2O_2* firstly occurred in the reaction steps and finally O_2 was desorbed from surface, with a minimum overpotential of 0.63 V (Fig. 8d). As shown in (Fig. 8b), the equilibrium potential in the most reasonable process was 2.54 V. In contrast, the graphene equilibrium potential was 2.20 V (shown in Fig. S7), and its charge transfer of 0.18e^- (Table S1) is also smaller than that of Co-N_4 (0.25e^-) when LiO_2* was adsorbed on its surface, which indicated the improved catalytic effect of Co-N_4 as shown in (Fig. 8d).

In a typical positive reaction of LOBs, the interactions between the intermediate product, final product and the catalytic active sites determine the overpotential and discharge capacity of the overall reaction. A higher adsorption energy represents a stronger interaction between the product and the catalyst surface, which could enhance the electron transfer and discharge capacity. (Fig. 9a) shows the binding energy of the intermediate LiO_2* and discharge product Li_2O_2* on graphene, (111) face of Co metal and single atom Co-N_4 sites. The binding energy of Co-N_4 sites with LiO_2* molecule is -0.66 eV, which is higher than that of single-layer graphene, and much lower than Co (111) crystal plane. The binding energy of the discharge product

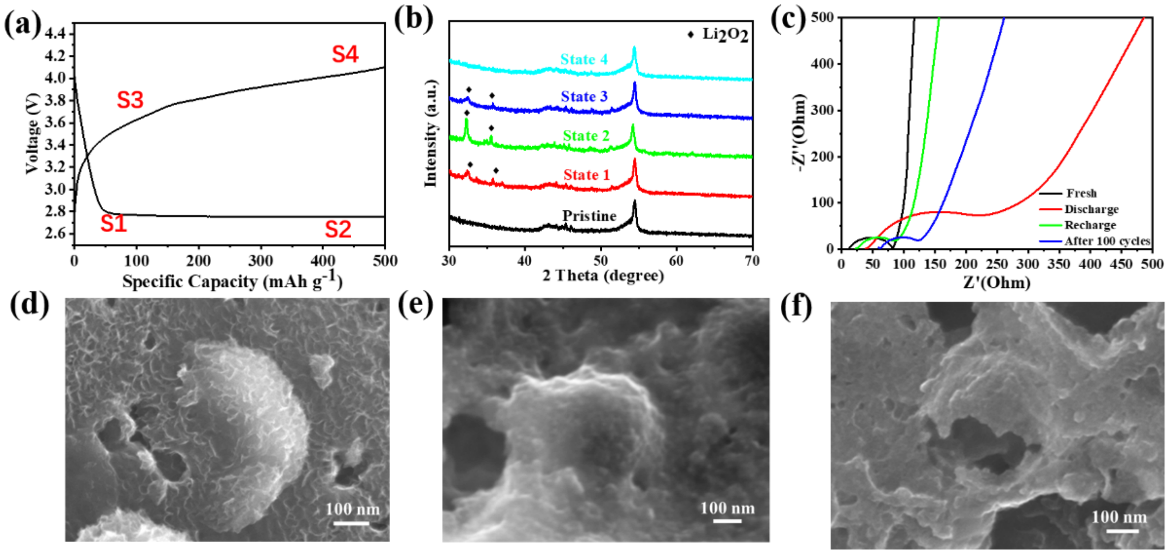

Fig. 7 (a) The selected states in a capacity-limited discharge and charge process; (b) XRD at different states of ACoNC-2 for the cathode and corresponding (d-f) SEM images after discharge, charge and 100 cycles; (c) EIS spectra.

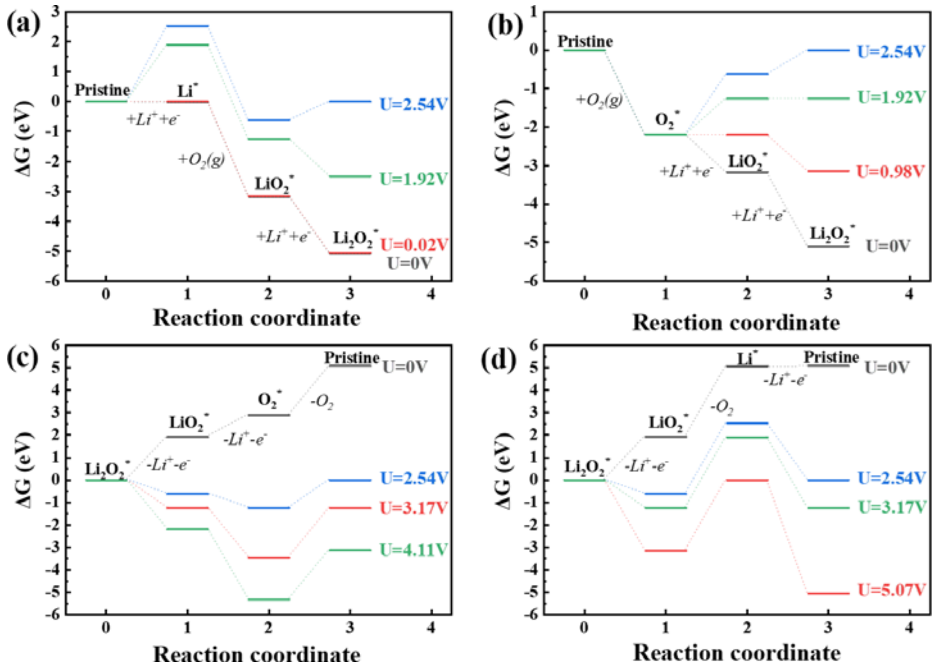

Fig. 8 The calculated energy diagrams of ORR (a, b) and OER (c, d) processes in two different paths on the Co-N_4 site.

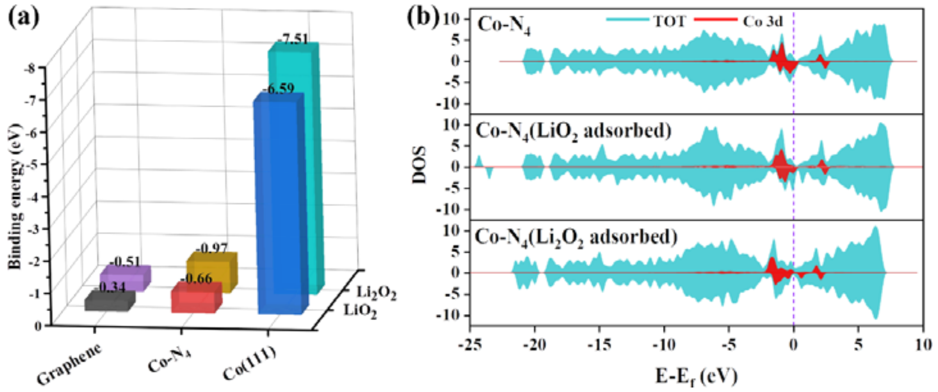

Fig. 9 (a) Comparison of binding energies of LiO_2 and Li_2O_2 at different active sites. Binding energy of Li_2O_2 adsorbed on Co (111) from Ref.41 and other data are in this work. (b) Density of states (DOS) of different adsorbates on Co-N_4 and corresponding projected density of states (PDOS) of Co-3d.

Li_2O_2* has the same binding energy sequence. To further analyze the adsorption between Co-N_4 and the product, the projected density of states (DOS) under different adsorbates are calculated (Fig. 9b). As the ORR reaction progresses, the electronic state gradually changes, and the DOS of the Fermi level decreases significantly after the adsorption of lithium peroxide, indicating that the conductivity is gradually weakened. Simultaneously, new bonds appear between adsorbates and substrate, as shown in (Fig. 10). However, due to the small charge transfer of Li_2O_2* (0.25 e^-), large distance (2.25 Å, Table S1) to the Co-N_4 site and the relatively low binging energy of the discharge products Li_2O_2*, it can be concluded that the adsorption of discharge product during the ORR/OER process for ACoNC catalyst is an extremely weak chemical adsorption. This weak chemical adsorption is not good for the mass and electron transfer during the cycling compared to that of Co metal and may contribute to the rapid decrease of the cycle stability at a high limited capacity and the rapid increase of overpotential during the cycling as shown in (Fig. 5).

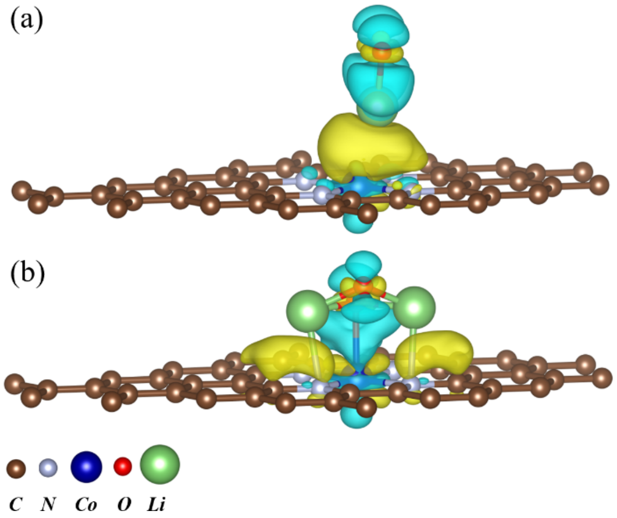

Fig. 10 Charge density difference of different adsorbates on Co-N_4. (a) LiO_2; (b) Li_2O_2.

4. Conclusions

In summary, single atom Co-N-C catalyst with a hierarchical porous structure was prepared through acid etching of Co/Co-N-C intermediate and tested as the cathode materials for LOBs. The cobalt atoms were anchored on the carbon matrix in the form of Co-N_4. The ACoNC catalyst achieved a large specific capacity of 14075 mAh g^{-1} and excellent recycle stability of 340 cycles with a fixed capacity of 500 mAh g^{-1} at a current of 100 mA g^{-1}. The discharge product film was identified on the surface of ACoNC catalyst. DFT simulation indicated that the formation and decomposition of discharge product is based on formation and adsorption of LiO_2 intermediate. Furthermore, the weak chemical adsorption of both intermediate and discharge product was identified by the theoretical simulation. Although weak chemical adsorption can maintain the stability of the Co-N_4 single atom active sites during the cycling, it may limit the mass and electron transfer in the ORR/OER process and contribute to the low cycle performance at a large fixed capacity.

Acknowledgements

This work was supported by National Key R&D Program of China of 2017YFE0195200 and 2018YFE0103500, Open Program of Guangxi Key Laboratory of Information Materials (171002-K) and the China Scholarship Council.

Supporting information

Available at https://dx.doi.org/10.30919/es8d1005

Conflict of interest

There are no conflicts to declare.

Reference

[1] M. Balaish, J.-W. Jung, I.-D. Kim and Y. Ein-Eli, *Adv. Funct. Mater.*, 2019, **201808303**, doi: 10.1002/adfm.201808303.

[2] C. Hou, J. Wang, W. Du, J. Wang, Y. Du, C. Liu, J. Zhang, H. Hou, F. Dang, L. Zhao and Z. Guo, *J. Mater. Chem. A*, 2019, **7**, 13460-13472, doi: 10.1039/c9ta03551f.

[3] C. Hou, Z. Tai, L. Zhao, Y. Zhai, Y. Hou, Y. Fan, F. Dang, J. Wang and H. Liu, *J. Mater. Chem. A*, 2018, **6**, 9723-9736, doi: 10.1039/ C8TA02863J

[4] J. B. Park, S. H. Lee, H. G. Jung, D. Aurbach and Y. K. Sun, *Adv. Mater.*, 2018, **30**, 1704162, doi: 10.1002/adma.201704162

[5] W. Chen, Y.-F. Gong and J.-H. Liu, *Chin. Chem. Lett.*, 2017, **28**, 709-718, doi: 10.1016/j.cclet.2016.10.023.

[6] L. Ma, T. Yu, E. Tzoganakis, K. Amine, T. Wu, Z. Chen and Lu, *Adv. Energy Mater.*, 2018, **8**, 1800348, doi: 10.1002/aenm.201800348

[7] J. Lu, L. Li, J. B. Park, Y. K. Sun, F. Wu and K. Amine, *Chem. Rev.*, 2014, **114**, 5611-5640, doi: 10.1021/cr400573b.

[8] X. Li, J. Huang and A. Faghri, *J. Power Sources*, 2016, **332**, 420-446, doi: 10.1016/j.jpowsour.2016.09.127.

[9] F. Soavi, S. Monaco and M. Mastragostino, *J. Power Sources*, 2013, **224**, 115-119, doi: 10.1016/j.jpowsour.2012.09.095

[10] J. Xie, X. Yao, Q. Cheng, I. P. Madden, P. Dornath, C. C. Chang, W. Fan and D. Wang, *Angew. Chem. Int. Ed. Engl.*, 2015, **54**, 4299- 4303, doi: 10.1002/anie.201410786.

[11] Z.-L. Wang, D. Xu, J.-J. Xu, L.-L. Zhang and X.-B. Zhang, *Adv. Funct. Mater.*, 2012, **22**, 3699-3705, doi: 10.1002/adfm.20120 0403.

[12] M. M. Ottakam Thotiyl, S. A. Freunberger, Z. Peng and P. G. Bruce, *J. Am. Chem. Soc.*, 2013, **135**, 494-500, doi: 10.1021/ja310258x

[13] S. Ma, Y. Wu, J. Wang, Y. Zhang, Y. Zhang, X. Yan, Y. Wei, P. Liu, J. Wang, K. Jiang, S. Fan, Y. Xu and Z. Peng, *Nano Lett.*, 2015, **15**, 8084-8090, doi: 10.1021/acs.nanolett.5b03510.

[14] F. Tu, J. Xie, S. Zhang, G. Cao, T. Zhu and X. J. Zhao, *J. Mater. Chem. A.*, 2015, **3**, 5714-5721, doi: 10.1039/c4ta06850e.

[15] X. Luo, M. Piernavieja-Hermida, J. Lu, T. Wu, J. Wen, Y. Ren, D. Miller, Z. Z. Fang, Y. Lei and K. J. Amine, *Nanotechnology*, 2015, **26**, 164003, doi: 10.1088/0957-4484/26/16/164003

[16] J. Liu, R. Younesi, T. Gustafsson, K. Edström and J. Zhu, *Nano Energy*, 2014, **10**, 19-27, doi: 10.1016/j.nanoen.2014.08.022.

[17] C. Hou, J. Wang, W. Zhang, J. Li, R. Zhang, J. Zhou, Y. Fan, D. Li, F. Dang, J. Liu, Y. Li, K. Liang and B. Kong, *ACS Appl. Mater. Inter.*, 2020, **12**, 13770-13780, doi: 10.1021/acsami.9b20317.

[18] J. Huang, B. Zhang, Y. Y. Xie, W. W. K. Lye, Z.-L. Xu, S. Abouali, M. A. Garakani, J.-Q. Huang, T.-Y. Zhang and B. J. C. Huang, *Carbon*, 2016, **100**, 329-336, doi: 10.1016/j.carbon.2016. 01.012

[19] Q. He, Q. Li, S. Khene, X. Ren, F. E. López-Suárez, D. Lozano-Castelló, A. Bueno-López and G. Wu, *J. Phys. Chem. C*, 2013, **117**, doi: 8697-8707, 10.1021/jp401814f.

[20] J. L. Shui, N. K. Karan, M. Balasubramanian, S. Y. Li and D. J. Liu, *J. Am. Chem. Soc.*, 2012, **134**, 16654-16661, doi: 10.1021/ja3042993.

[21] H. Zhong, Y. Luo, S. He, P. Tang, D. Li, N. Alonso-Vante and Y. Feng, *ACS Appl. Mater. Interfaces*, 2017, **9**, 2541-2549, doi: 10.1021/acsami.6b14942.

[22] C. Zhu, S. Fu, J. Song, Q. Shi, D. Su, M. H. Engelhard, X. Li, D. Xiao, D. Li, L. Estevez, D. Du and Y. Lin, *Small*, 2017, **13**, doi: 10. 1002/smll.201603407.

[23] H. Zhang, S. Hwang, M. Wang, Z. Feng, S. Karakalos, L. Luo, Z. Qiao, X. Xie, C. Wang, D. Su, Y. Shao and G. Wu, *J. Am. Chem. Soc.*, 2017, **139**, 14143-14149, doi: 10.1021/jacs.7b0 6514.

[24] W. Zang, A. Sumboja, Y. Ma, H. Zhang, Y. Wu, S. Wu, H. Wu, Z. Liu, C. Guan and J. Wang, *ACS Catal.*, 2018, **8**, 8961-8969, doi: 10.1021/acscatal.8b02556.

[25] C. Gao, S. Chen, Y. Wang, J. Wang, X. Zheng, J. Zhu, L. Song, W. Zhang and Y. Xiong, *Adv. Mater.*, 2018, **30**, doi: 10.1002/ adma.201704624.

[26] L. Yang, L. Shi, D. Wang, Y. Lv and D. Cao, *Nano Energy*, 2018, **50**, 691-698, doi: 10.1016/j.nanoen.2018.06.023.

[27] X. Cui, J. Xiao, Y. Wu, P. Du, R. Si, H. Yang, H. Tian, J. Li, W.-H. Zhang, D. Deng and X. Bao, *Angew. Chem. Int. Ed.*, 2016, **55**, 6708-6712, doi: 10.1002/anie.201602097.

[28] H. Fei, J. Dong, M. J. Arellano-Jiménez, G. Ye, N. Dong Kim, E. L. G. Samuel, Z. Peng, Z. Zhu, F. Qin, J. Bao, M. J. Yacaman, P. M. Ajayan, D. Chen and J. M. Tour, *Nat. Commu.*, 2015, **6**, 1-8, doi: 10.1038/ncomms9668.

[29] G. Kresse and J. Furthmuller, *Phys. Rev. B*, 1996, **54**, 11169-11186, doi: 10.1103/PhysRevB.54.11169.

[30] G. Kresse and J. Furthmuller, *Comput. Mater. Sci.*, 1996, **6**, 15-50, doi: 10.1016/0927-0256(96)00008-0.

[31] J. P. Perdew, K. Burke and M. Ernzerhof, *Phys. Rev. Lett.,* 1996, **77**, 3865-3868, doi: 10.1103/PhysRevLett.77.3865.

[32] Y. Han, Z. Wang, R. Xu, W. Zhang, W. Chen, L. Zheng, J. Zhang, J. Luo, K. Wu, Y. Zhu, C. Chen, Q. Peng, Q. Liu, P. Hu, D. Wang and Y. Li, *Angew. Chem. Int. Ed. Engl.,* 2018, **57**, 11262-11266, doi: 10.1002/anie.201805467.

[33] Y. Zhu, W. Sun, W. Chen, T. Cao, Y. Xiong, J. Luo, J. Dong, L. Zheng, J. Zhang, X. Wang, C. Chen, Q. Peng, D. Wang and Y. Li, *Adv. Functi. Mater.,* 2018, **28**, doi: 10.1002/adfm. 201802167.

[34] J. K. Norskov, J. Rossmeisl, A. Logadottir, L. Lindqvist, J. R. Kitchin, T. Bligaard and H. Jonsson, *J. Phys. Chem. B,* 2004, **108**, 17886-17892, doi: 10.1021/jp047349j.

[35] J. Zhu, X. Ren, J. Liu, W. Zhang and Z. Wen, *ACS Catal.,* 2014, **5**, 73-81, doi: 10.1021/cs5014442.

[36] R. F. W. Bader, *Atoms in Molecules: A Quantum Theory*. Oxford University Press: New York, 1990, vol. **360**.

[37] A. Arnaldsson and H. Jonsson, *Comput. Mater. Sci.,* 2006, **36**, 354-360, doi: 10.1016/j.commatsci.2005.04.010.

[38] W. Tang, E. Sanville and G. Henkelman, *J.Phys.: Condens. Matter,* 2009, **21**, 084204, doi: 10.1088/0953-8984/21/8/084204.

[39] Y. Hou, J. Wang, J. Liu, C. Hou, Z. Xiu, Y. Fan, L. Zhao, Y. Zhai, H. Li, J. Zeng, X. Gao, S. Zhou, D. Li, Y. Li, F. Dang, K. Liang, P. Chen, C. Li, D. Zhao and B. Kong, *Adv. Energy Mater.,* 2019, **9**, doi: 10.1002/aenm.201901751.

[40] B. He, J. Wang, Y. Fan, Y. Jiang, Y. Zhai, Y. Wang, Q. Huang, F. Dang, Z. Zhang and N. Wang, *J. Mater. Chem. A,* 2018, **6**, 19075-19084, doi: 10.1039/c8ta07185c.

[41] Y. Zhai, J. Wang, Q. Gao, Y. Fan, C. Hou, Y. Hou, H. Liu, Q. Shao, S. Wu and L. Zhao, *J. Catal.*, 2019, **377**, 534-542, doi: 10. 1016/j.jcat.2019.07.055.

[42] G. Sun, Q. Zhao, T. Wu, W. Lu, M. Bao, L. Sun, H. Xie and J. Liu, *ACS Appl. Mater. Interfaces,* 2018, **10**, 6327-6335, doi: 10.1021/ acsami.7b17795.

[43] G. Tan, L. Chong, R. Amine, J. Lu, C. Liu, Y. Yuan, J. Wen, K. He, X. Bi, Y. Guo, H. H. Wang, R. Shahbazian-Yassar, S. Al Hallaj, D. J. Miller, D. Liu and K. Amine, *Nano Lett.,* 2017, **17**, 2959-2966, doi: 10.1021/acs.nanolett.7b00207.

[44] T. Y. Wei, C. Y. Kuo, Y. J. Hsu, S. Y. Lu and Y. C. Chang, *Microporous Mesoporous Mater.*, 2008, **112**, 580-588,

[45] Liu, Jian-Lin, Lin and Ren-Bin. *Powder Technol.*, 2013, **241**, 188- 195, doi: 10.1016/j.powtec.2013.03.022.

[46] L. Sun, J. Tuo, M. Zhang, C. Wu, Z. Wang and Y. J. F. Zheng, *Fuel*, 2015, **158**, 549-557, doi: 10.1016/j.fuel.2015.05.061

[47] M. J. Song, I. T. Kim, Y. B. Kim and M. W. Shin, *Electrochim. Acta,* 2015, **182**, 289-296, doi: 10.1016/j.electacta.2015.09.100.

[48] Z. Zhang, Y. Chen, J. Bao, Z. Xie, J. Wei and Z. Zhou, *Part. Part. Syst. Charact.,* 2015, **32**, 680-685, doi: 10.1002/ppsc.201400242.

[49] M. Yuan, L. Lin, Y. Yang, C. Nan, S. Ma, G. Sun and H. Li, *Nanotechnology,* 2017, **28**, 185401, doi: 10.1088/1361-6528/aa66bc.

[50] X. X. Wang, D. A. Cullen, Y. T. Pan, S. Hwang, M. Wang, Z. Feng, J. Wang, M. H. Engelhard, H. Zhang, Y. He, Y. Shao, D. Su, K. L. More, J. S. Spendelow and G. Wu, *Adv. Mater.,* 2018, **30**, doi: 10.1002/adma.201706758.

[51] Zhang, X., Ziemer, K.S. & Weeks, B.L., *Adv. Compos. Hybrid Mater.*, 2019, **2**, 492-500, doi: 10.1007/s42114-019-00113-8.

[52] B. He, J. Wang, J. Liu, Y. Li, Q. Huang, Y. Hou, G. Li, J. Li, R. Zhang, J. Zhou, W. Tian, Y. Du, F. Dang, H. Wang and B. Kong, *Adv. Energy Mater.,* 2020, doi: 10.1002/aenm.201904262.

[53] Y. Wang, J. Wang, Z. Mohamed, Q. Huang, T. Chen, Y. Hou, F. Dang, W. Zhang and H. Wang, *Appl. Mater. Today,* 2020, **19**, 100603, doi: 10.1016/j.apmt.2020.100603.

[54] Y. Bae, D.-H. Ko, S. Lee, H.-D. Lim, Y.-J. Kim, H.-S. Shim, H. Park, Y. Ko, S. K. Park, H. J. Kwon, H. Kim, H.-T. Kim, Y.-S. Min, D. Im and K. Kang, *Adv. Energy Mater.*, 2018, **8**, 1702661, doi: 10.1002/aenm.201702661.

[55] D. Kundu, R. Black, E. J. m. Berg and L. F. *Energy Environ. Sci.*, 2015, **8**, 1292-1298, doi: 10.1039/C4EE02587C

[56] S. M. Ahn, J. Suk, D. Y. Kim, Y. Kang, H. K. Kim and D. W. Kim, *Adv. Sci.,* 2017, **4**, 1700235, doi: 10.1002/advs.201700235.

[57] J. Xu, J. Wu, L. Luo, X. Chen, H. Qin, V. Dravid, S. Mi and C. Jia, *J. Power Sources*, 2015, **274**, 816-822, doi: 10.1016/j. jpowsour. 2014.10.106.

[58] E. Jokar, A. I. Zad and S. Shahrokhian, *J. Solid State Electrochem.*, 2015, **19**, 269-274, doi: 10.1007/s10008-014-2592-y.

[59] L. Wang, M. Ara, K. Wadumesthrige, S. Salley and K. Y. S. Ng, *J. Power Sources*, 2013, **234**, 8-15, doi: 10.1016/j.jpowsour.2013. 01. 037.

[60] K. P. C. Yao, D. G. Kwabi, R. A. Quinlan, A. N. Mansour, A. Grimaud, Y.-L. Lee, Y.-C. Lu and Y. Shao-Horn, *J. Electrochem. Soc.*, 2013, **160**, A824-A831, doi: 10.1149/2.069306jes.

[61] Y. Hou, J. Wang, C. Hou, Y. Fan, Y. Zhai, H. Li, F. Dang and S. Chou. *J. Mater. Chem. A*, 2019, **7**, 6552-6561, doi: 10.1039/c9ta 00882a.

[62] R. Choi, J. Jung, G. Kim, K. Song, Y.-I. Kim, S. C. Jung, Y.-K. Han, H. Song and Y.-M. Kang, *Energy Environ. Sci.,* 2014, **7**, doi: 10.1039/c3ee43437k.

[63] Y. Jing and Z. Zhou, *ACS Catal.,* 2015, **5**, 4309-4317, doi: 10. 1021/acscatal.5b00332.

[64] H.-J. Kim, S. C. Jung, Y.-K. Han and S. H. Oh, *Nano Energy,* 2015, **13**, 679-686, doi: 10.1016/j.nanoen.2015.03.030.

[65] L. Shi, A. Xu and T. Zhao, *J. Phys. Chem. C,* 2016, **120**, 6356-6362, doi: 10.1021/acs.jpcc.6b00014.